

cambridge.org/mrf

K. Lomakin , L. Klein and G. Gold

Institute of Microwaves and Photonics, Friedrich-Alexander University Erlangen-Nuremberg, Erlangen, Germany

## Research Paper

**Cite this article:** Lomakin K, Klein L, Gold G (2021). Design and analysis of 3D-printed hybrid couplers for D-band applications. *International Journal of Microwave and Wireless Technologies* **13**, 719–726. <https://doi.org/10.1017/S1759078721000647>

Received: 6 November 2020

Revised: 2 April 2021

Accepted: 7 April 2021

First published online: 11 May 2021

### Keywords:

3D printing; additive manufacturing; D-band hybrid coupler; electroless plating; manufacturing tolerances; slotted waveguides

### Author for correspondence:

K. Lomakin,

E-mail: [konstantin.lomakin@fau.de](mailto:konstantin.lomakin@fau.de)

## Abstract

This work focuses on the impact of the build orientation on additively manufactured waveguide-based hybrid couplers for D-band frequency range and relates it to other sources of uncertainty within the overall manufacturing process and measurement instrumentation for the D-band frequency range. The designed specimens are first printed from UV curable photopolymer resin and subsequently metal coated by an electroless silver plating process, which in turn is improved by making use of the slotted waveguide approach. Although the requirements toward geometrical precision to achieve phase errors below  $10^\circ$  are in an order of 0.1 mm, a desktop grade DLP printer is utilized in this work in order to point out the prospects and limitations of additive manufacturing. Furthermore, waveguide paths with bends are part of the model and their impact on the measured attenuation is estimated explicitly.

Despite this narrow field of tolerances, one specimen could have been realized, which achieves a measured output magnitude imbalance of 0.7 dB over the frequency range from 120 to 155 GHz while at the same time exhibiting a phase deviation of only  $<10^\circ$  from the desired  $90^\circ$ . With these demonstrated results, the proposed approach provides suitability for future applications in the D-band frequency range.

## Introduction

Technological trends, such as autonomous driving or next generation of communication standards, provide a wide range of applications for mm-Wave components and systems. However, with ever increasing frequencies, limitations of conventional manufacturing technologies become a bottleneck for the achievable system performance and design effort. While printed circuit board (PCB) solutions suffer from dielectric loss which in turn scales linearly with frequency, waveguide solutions are typically bulky and rather expensive due to the laborious milling process. Moreover, with increasing system complexity, the typically utilized split block assembly [1] turns into a complex puzzle and the requirements of the next higher ISM-band for automotive radar sensors – probably operating at 140 GHz – impose additional challenges on the milling and assembly precision.

In this context, additive manufacturing is an interesting alternative as it combines an inherent geometrical freedom with relatively cost-efficient machinery and manufacturing. Among a wide range of different 3D printing concepts available on the market, stereolithography and digital light processing (DLP) offer the required geometrical precision in a range of 50–100  $\mu\text{m}$  while at the same time, yielding a decent surface quality below 1  $\mu\text{m}$  RMS-surface roughness [2], which is mandatory for the D-band frequency range [3]. Yet, the mostly utilized UV photo-polymer resins must be subsequently metal plated in order to provide the desired functionality of a hollow waveguide component, which can be done by applying electroplating [4]. However, with complex structures, undercuts, and hollow cavities, the electroplating may become a challenge as well.

In order to overcome this drawback, an electroless silver plating process has been refined and proposed in [5, 6]. By replacing the hollow waveguide structure with the so-called slotted waveguides [2, 6], where the narrow walls are assembled by posts instead of continuous walls similar to substrate-integrated waveguides, the metal plating process can be significantly improved, which in turn allows for the realization of complex waveguide components such as couplers [7] and even helix antennas [8] in E-band.

Recently, this approach has been proved in principal even for D-band at straight waveguides [9] and hybrid couplers [10]. Yet, the required level of precision in this region becomes a challenge for desktop grade DLP printers as well which led to relatively large undesired phase deviation between the coupling and through output ports in [10]. Furthermore, measurement instrumentation and extension structures, such as additional waveguide sections for the connection of instruments, represent another source of impact on the measured attenuation levels of the coupling region itself. Therefore, this work focuses on the analysis of the impact of both, the measurement instrumentation and the manufacturing tolerances on the realized coupler

© The Author(s), 2021. Published by Cambridge University Press in association with the European Microwave Association. This is an Open Access article, distributed under the terms of the Creative Commons Attribution-NonCommercial-ShareAlike licence (<http://creativecommons.org/licenses/by-nc-sa/4.0/>), which permits non-commercial re-use, distribution, and reproduction in any medium, provided the same Creative Commons licence is included and the original work is properly cited. The written permission of Cambridge University Press must be obtained for commercial re-use.

**CAMBRIDGE**  
UNIVERSITY PRESS

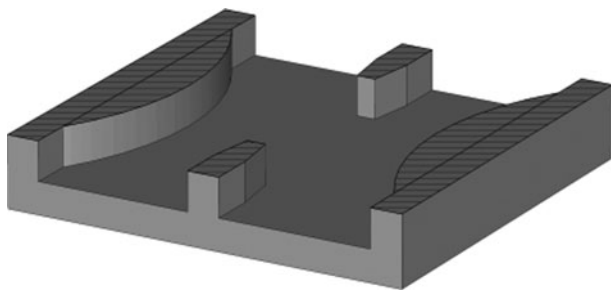


Fig. 1. Minimal CAD model for optimization of coupling region.

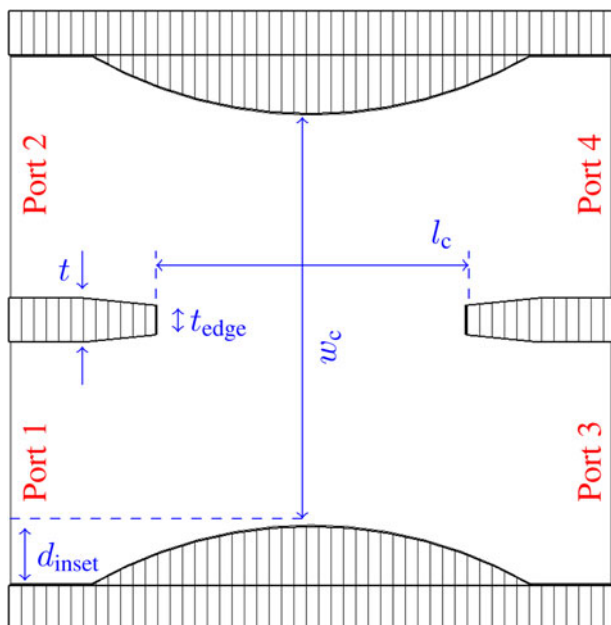


Fig. 2. Cross-section of the optimized simulation model.

performance explicitly for the range between 110 and 170 GHz with desktop grade DLP printing systems.

### Simulation-based optimization tolerance analysis

In order to find an optimal geometry for a 90° hybrid coupler, a minimal model containing only the critical coupling region is designed in *CST Microwave Studio*, which is shown in Fig. 1. The cross-section including the set of parameters, which are used for parameter sweeps, is provided in Fig. 2, where the two cylindrical shapes that are inserted into the coupling region from both sides exhibit both the same radius  $r_{\text{inset}}$ . The conductor material is modeled as a rough surface exhibiting a bulk conductivity  $\sigma_{\text{DC}} = 10 \text{ MS/m}$  and an RMS surface roughness of  $R_q = 800 \text{ nm}$  based on prior work.

Some of the parameters, such as  $t_{\text{edge}}$  are bound within the manufacturing limitations of the utilized 3D printer, hence, it should not fall below  $200 \mu\text{m}$ . The optimal parameters acquired by simulation sweeps are shown in Table 1.

However, deviations from the optimum values are expected in the 3D-printed specimen due to tolerances of the 3D printer. Although the final precision depends on many aspects of the manufacturing process including the choice of resin, cleaning,

Table 1. Overview of geometrical parameters as optimized by simulation

| Parameter          | Value, mm |
|--------------------|-----------|
| $t$                | 0.3       |
| $t_{\text{edge}}$  | 0.2       |
| $l_c$              | 2.1       |
| $w_c$              | 2.8       |
| $d_{\text{inset}}$ | 0.4       |
| $r_{\text{inset}}$ | 3.0       |

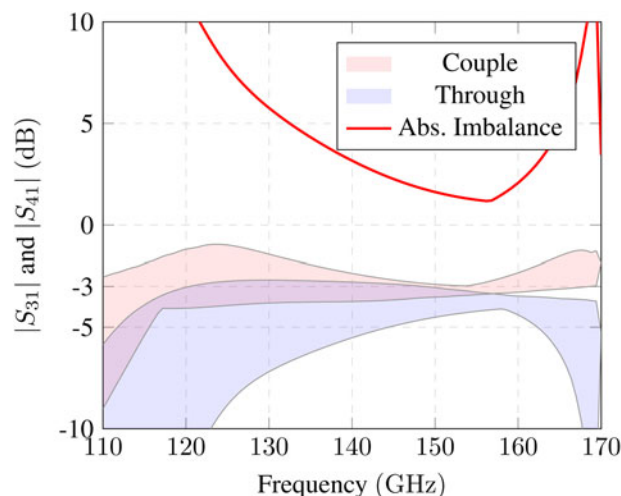
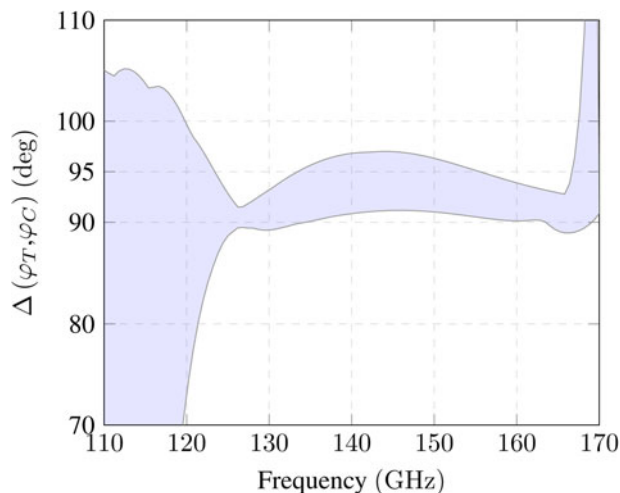


Fig. 3. Maximum range of simulated Through and Couple paths for variation of  $\pm 50 \mu\text{m}$  within critical geometry of coupling region ( $l_c$ ,  $d_{\text{inset}}$ ,  $t$ , and  $t_{\text{edge}}$ ) in Fig. 1.

and curing settings as well as the printer resolution itself, it has been shown [11] that a relative error  $\leq 3.3\%$  and – depending on the orientation – even  $\leq 1.8\%$  can be achieved with a printer of nominal  $30 \mu\text{m}$  resolution in  $xy$ -plane.

Measurements in [10] suggest deviations in the order of  $\pm 50 \mu\text{m}$  along the critical geometry of the coupling region in Fig. 2 which resembles a relative deviation of approximately 1–5% and is in line with the utilized machine resolution of  $50 \mu\text{m}$  in  $xy$ -plane and  $10 \mu\text{m}$  in  $z$ -direction. Hence, parameter sweeps with the model in Fig. 2 for  $l_c$ ,  $d_{\text{inset}}$ ,  $t$ , and  $t_{\text{edge}}$  varying each within  $\pm 50 \mu\text{m}$  are evaluated to visualize the worst-case impact of imperfections in the coupling region without taking the waveguide connections into account. Therefore, Fig. 3 shows the simulated range for through ( $S_{31}$ ) and couple ( $S_{41}$ ) paths as well as the maximum imbalance in magnitude ( $\|S_{31}\| - \|S_{41}\|$ ) among all combinations. Within the range from 132 to 165 GHz, the worst-case imbalance remains below 5 dB. The corresponding impact of such variations in geometry on the phase difference at the output ports between  $S_{31}$  and  $S_{41}$  is summarized in Fig. 4, where the phase deviates by only  $7^\circ$  within the frequency range from 130 to 165 GHz in worst-case combination of geometry variation.

Since the minimal model cannot be directly measured due to the size of the measurement equipment, test fixtures need to be designed in order to attach the coupling region to the measurement interface – which in turn should finally be realized as a standard WR06 flange connection. Therefore, Fig. 5 shows the extended simulation model, where continuous wall waveguide



**Fig. 4.** Maximum range of simulated phase difference at output between  $S_{31}$  and  $S_{41}$  for variation of  $\pm 50 \mu\text{m}$  within critical geometry of coupling region ( $l_c$ ,  $d_{\text{inset}}$ ,  $t$ , and  $t_{\text{edge}}$ ) in Fig. 1.

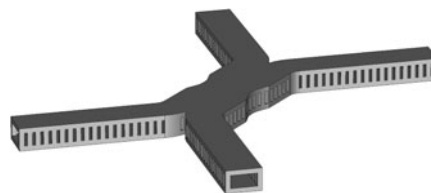


**Fig. 5.** CAD model for simulation including waveguide test fixture.

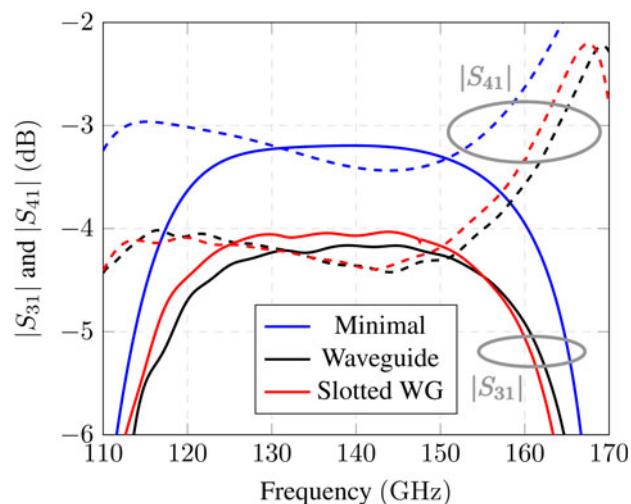
paths are added to account for the necessary test fixture. Since the final specimens will be fabricated following the slotted waveguide approach [2, 6, 7], where the waveguide is implemented similar to an SIW with regular posts miming a continuous wall, another rather complex simulation model is proposed in Fig. 6. Therein, the previously continuous narrow walls are resembled by posts with a thickness of  $d = 350 \mu\text{m}$  and a periodicity  $s = 500 \mu\text{m}$ . The same material properties are deployed in all three cases.

Figure 7 shows the simulated insertion losses along the through ( $|S_{31}|$ ) and couple ( $|S_{41}|$ ) paths for the three presented simulation models. While the minimal model achieves about 0.3 dB less than the ideal  $-3 \text{ dB}$  due to conductor loss and surface roughness along the short coupling region, both complex models drop down toward  $-4.3 \text{ dB}$  due to the losses along the test fixtures. However, there is no significant difference between the continuous wall and the slotted waveguide model, and in all cases, the imbalance in output magnitude at through and couple paths remains within the same order.

The test fixture waveguides are in turn prone to tolerances within printing and handling, which may have significant impact on the performance due to the relatively long waveguide sections. A dimensional mismatch between the different waveguide paths – which may be related to an asymmetric distortion of the model due to non-homogeneous shrinking – causes a deviation of the output phase  $\Delta\varphi_{\text{TC}}$  between the through and coupling path from the ideal  $90^\circ$ . This impact is simulated in CST in order to provide an estimation on the overall precision that can be realized with desktop grade printing systems in the D-band frequency range. Therefore, port 3 of the minimal model is extended by a short variable waveguide section, which is swept by simulation



**Fig. 6.** CAD model for simulation including slotted waveguide test fixture.



**Fig. 7.** Comparison of different simulation setups with: continuous line  $\Leftrightarrow S_{31}$  and dashed line  $\Leftrightarrow S_{41}$ .

within a range from 0 to  $300 \mu\text{m}$ . This setup is identical to an asymmetry within the test fixture paths of the complex models and can be spread along the entire model. The deviation of  $\Delta\varphi_{\text{TC}}$  from the ideal  $90^\circ$  is shown in Fig. 8. Obviously, an asymmetry as little as  $100 \mu\text{m}$  can already lead to a phase error of  $> 10^\circ$ , therefore, imposing a tough challenge for the manufacturing process even for conventional systems already. Furthermore, simulation suggests that asymmetry within the manufactured model has a significantly higher impact on the phase deviation than symmetrical tolerances within the coupling region itself, while symmetric ones have, in turn, a more significant impact on the magnitude imbalance.

### Design for manufacturing and manufactured specimens

As previously indicated, the minimal model of the coupling region is extended by test fixtures and flanges for measurement purpose. Since the model should be kept as small as possible to avoid losing too much precision on the attenuation within the waveguide sections, the flanges are attached in an angle of  $45^\circ$  to the model to provide space for the frequency converters in the measurement assembly. Figure 9 shows the CAD model of the proposed coupler that includes the particularly intersecting flanges and the slotted waveguide sections. Furthermore, Fig. 10 provides a cross-section view on the manufacturing model, where especially the posts of the narrow waveguide walls can be seen.

Although the test fixtures are simulated including conductor loss and surface roughness, the final impact of printing and metal plating is rather difficult to simulate in advance.

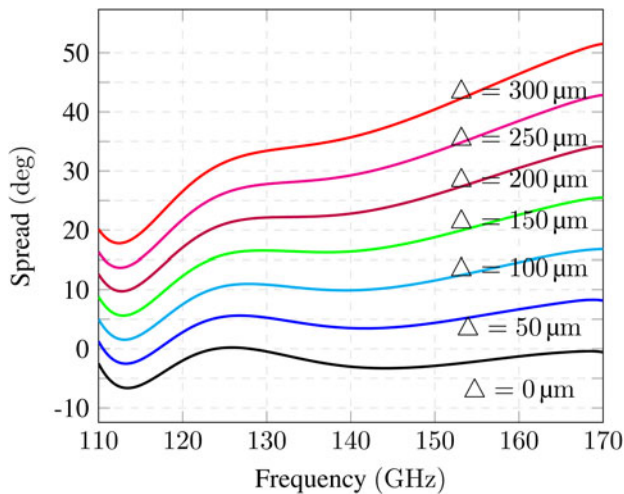


Fig. 8. Simulated deviation of phase difference from the ideal of  $90^\circ$  between through and couple ports due to asymmetry within path lengths.

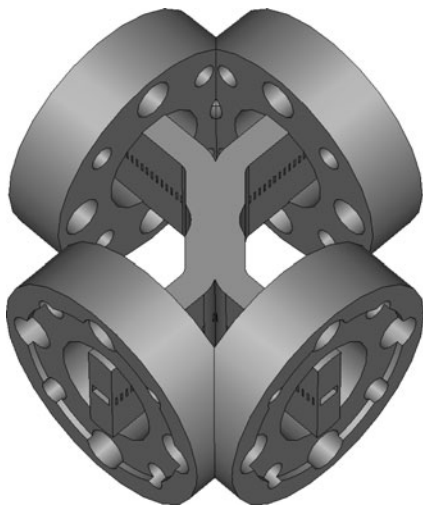


Fig. 9. Adjusted manufacturing model of the proposed hybrid coupler.

Therefore, a simple two-port model is designed as shown in Fig. 11 as a CAD-model and in Fig. 12 as manufactured part, where the test fixture sections are pointed straight onto each other – similar to a through-calibration structure for the case of measuring the coupling-path (e.g.  $S_{41}$ ). This model is manufactured by the same process as the actual specimens, but measured separately in order to get an estimation of the attenuation within the test fixture paths, which can afterwards be used to correct the coupler measurements.

Finally, the actual coupler model is printed in three different orientations (A, B, and C) as shown in Fig. 13. In case of A, all four ports are placed on the  $xy$ -plane of the printer, consequently, being parallel to the build platform. With orientation B, the model is rotated by  $90^\circ$  along the long side and placed on ports 1 and 3. Lastly, in case of C, the model is placed under a  $45^\circ$  angle against the  $xy$ -plane.

The utilized printer is a desktop grade DLP printer with a nominal  $xy$ -resolution of roughly  $50 \mu\text{m}$  and a  $z$ -axis accuracy of up to  $10 \mu\text{m}$ . After printing the plastic body, it is cleaned

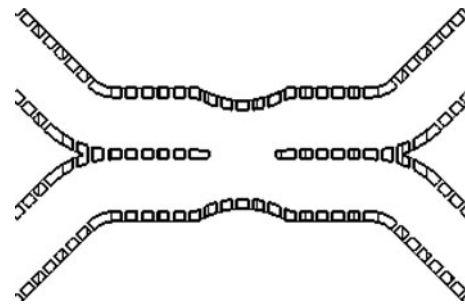


Fig. 10. Cross-section of the coupling region.

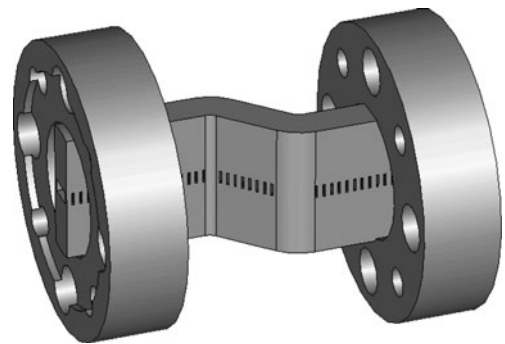


Fig. 11. Model for estimating attenuation of test fixture.



Fig. 12. Manufactured through-type structure for estimating attenuation of test fixture.

using isopropanol alcohol and post-processed in a UV-curing chamber followed by an electroless silver plating process, which in turn is repeated three times. One of the manufactured specimens is shown in Fig. 14.

### Estimation of test fixture attenuation and operational tolerances

Since the simulation of phase deviation suggests a high sensitivity toward small dimensional mismatch, high accuracy is required within the measurement. Hence, also the tolerances that are imposed by operation, especially the flange attachment, are analyzed. Therefore, the manufactured specimens are measured four times with different torques manually applied to the flanges, which is shown in Fig. 15, where the spread within the magnitude of the through and coupling path among the four different

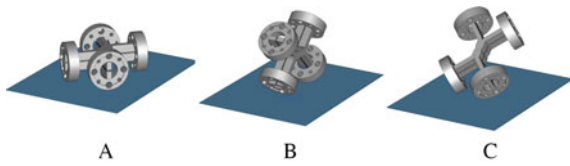


Fig. 13. Build orientations of specimens A, B, and C as considered in this work.

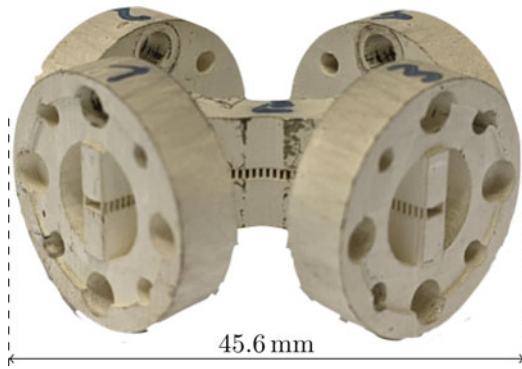


Fig. 14. One of the manufactured specimens (orientation A).

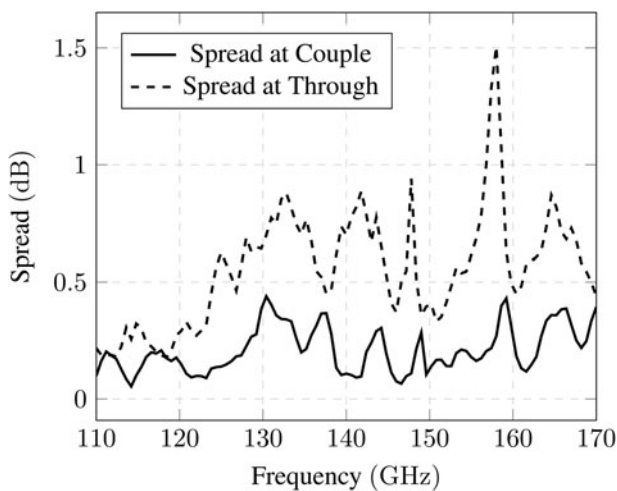


Fig. 15. Measured spread of through and couple path for variation of screw torque.

settings is plotted over frequency. It shows that the manual handling of screws at the flanges can lead to an error of up to 1 dB in magnitude since the utilized material has a certain elasticity and a relatively simple flange design is used, which relies on a plane face contact. Figure 16 shows the impact of flange attachment on the deviation of  $\Delta\varphi_{TC}$ , which can reach 15° when too little torque is applied or the flange alignment is not correct. Consequently, comparing these measurements to Fig. 8, handling the measurement setup can lead to a phase error which is similar to a geometry deviation of  $\approx 100 \mu\text{m}$  and moreover, even surpass the impact of geometry deviations within the coupling region as simulated in Fig. 4. However, the impact on the magnitude imbalance should remain within  $< 2 \text{ dB}$  and is therefore less critical as compared to the deviations within the coupling region as stated in Fig. 3.

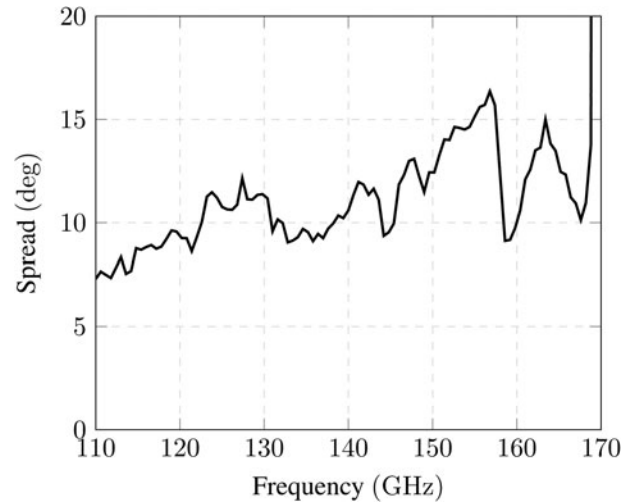


Fig. 16. Measured maximum spread of phase difference between through and couple path for variation of screw torque.

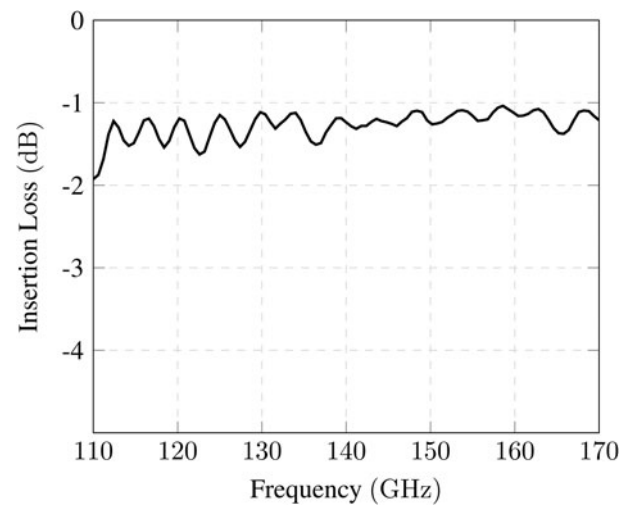
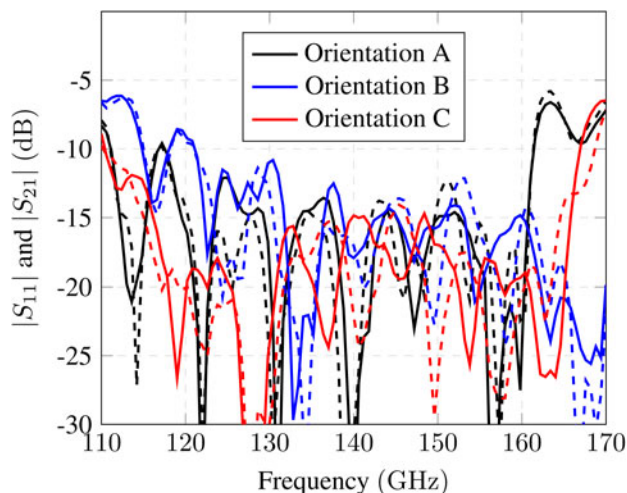


Fig. 17. Measured test fixture attenuation.

Finally, Fig. 17 shows the measured attenuation within the test fixture waveguide sections on both sides, which sum up to a value between  $-1$  and  $-1.5 \text{ dB}$  in the interesting frequency region which is in line with the simulation results in Fig. 7, where an additional attenuation of  $\approx 1 \text{ dB}$  is introduced between minimal and complex model. Consequently, an overall drop of around  $-1$  and  $-1.5 \text{ dB}$  below the ideal  $-3 \text{ dB}$  attenuation in through and couple path is expected in the measurement, while the magnitude imbalance between through and couple paths should not be affected due to symmetry in the design.

### Measurement and characterization

The three different coupler orientations A, B, and C are all measured at a VNA with D-band frequency converters that are calibrated to the flange interface by a TOSM algorithm with waveguide calibration standards. Since the four-port coupler is



**Fig. 18.** Measured matching  $|S_{11}|$  (solid) and isolation  $|S_{21}|$  (dashed) of the manufactured specimen for all orientation types A, B, and C.

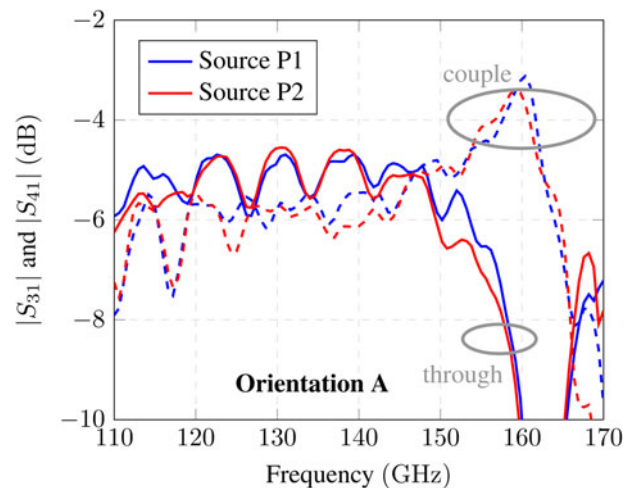
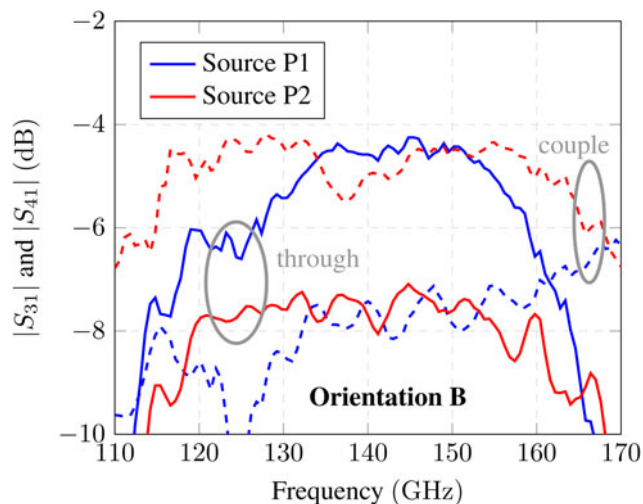


**Fig. 19.** Measured through (solid) and couple (dashed) path for source at ports 1 and 2 of specimen orientation type A.

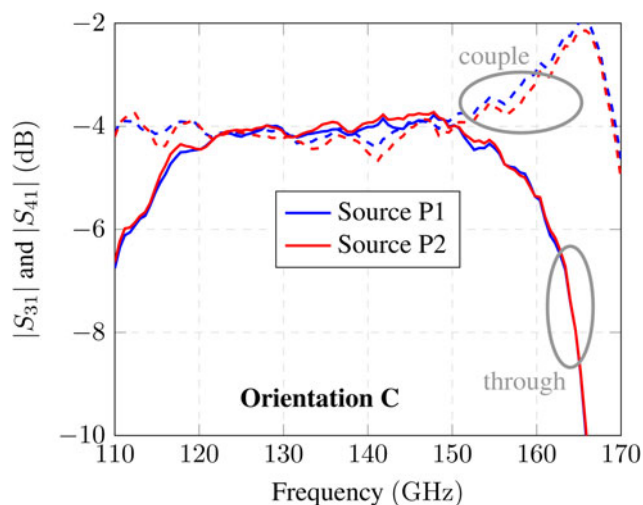
measured by a two-port measurement setup, the complete S-parameters are assembled from the respective permutations, while the other two ports are therefore terminated by waveguide matches.

Figure 18 shows the return- ( $|S_{11}|$ ) and isolation ( $|S_{21}|$ ) loss of the three specimen. Isolation and matching are in the same order of magnitude within each orientation and generally remain below  $-10$  dB within 120–160 GHz. Specimen C even achieves a  $-15$  dB-bandwidth from 116 to 165 GHz.

The measured magnitude of through and couple paths at each specimen (A, B, and C) for source at port 1 ( $|S_{41}|$  and  $|S_{31}|$ ) and source at port 2 ( $|S_{42}|$  and  $|S_{32}|$ ) is shown in Figs 19–21, respectively. As suggested by simulation in Fig. 7, the overall magnitude drops significantly toward  $-4\dots-6$  dB in case of A and C and even reaches  $-8$  dB in case of sample B. However, the general functionality of the hybrid coupler is still given in all three samples. Sample C is even almost identical to simulated responses with a deviation of  $<0.5$  dB as shown in the closeup comparison in Fig. 22. The magnitude imbalance between



**Fig. 20.** Measured through (solid) and couple (dashed) path for source at ports 1 and 2 of specimen orientation type B.



**Fig. 21.** Measured through (solid) and couple (dashed) path for source at ports 1 and 2 of specimen orientation type C.

through and couple output is summarized in Fig. 23 where sample C even remains within a narrow margin of  $\pm 0.7$  dB from 115 to 155 GHz, therefore, suggesting very high degree of accuracy and quality, while sample A also shows acceptable behavior. Moreover, considering the measured attenuation within the test fixture sections of 1–1.5 dB, the actual coupling region of coupler C even reaches almost ideal  $-3$  dB for through and coupling paths.

Similar results can be observed within the measured phase difference  $\Delta\varphi_{TC}$  between through and couple output paths for source at port 1 and 2 respectively as shown in Figs 24–26 for all three specimens. While sample B defines a range around the desired  $90^\circ$  from  $50^\circ$  to  $120^\circ$  – hence, spanning  $70^\circ$  – sample C achieves a very narrow range from  $80^\circ$  to  $94^\circ$  from 120 to 160 GHz, leaving sample A in between. Consequently, build orientation C allows for a realized precision that is in the order of the phase tolerances imposed by manual handling of flange interconnections and resembles a geometrical asymmetry within the narrow margin of  $\approx 100$   $\mu\text{m}$  as indicated by the simulated

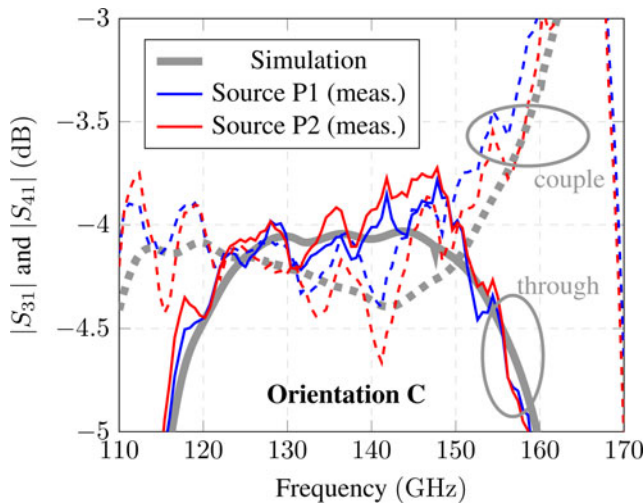


**Fig. 22.** Closeup on measured through (solid) and couple (dashed) path for source at ports 1 and 2 of specimen orientation type C compared with simulation results for slotted WG from Fig. 7.

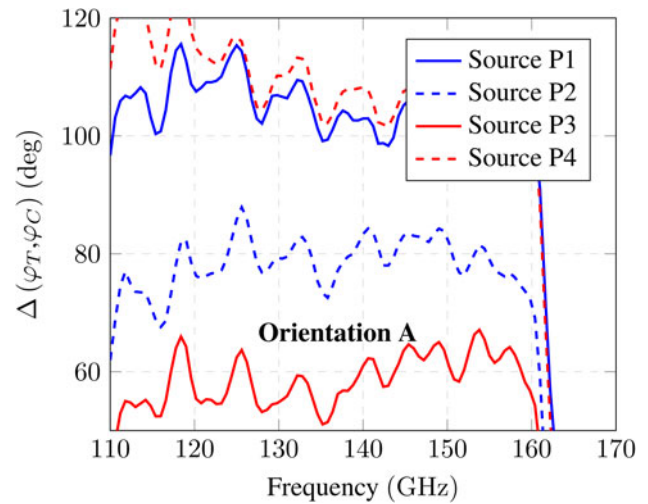


**Fig. 24.** Measured phase difference between through and coupling paths for source at ports 1, 2, 3, and 4 of specimen A.

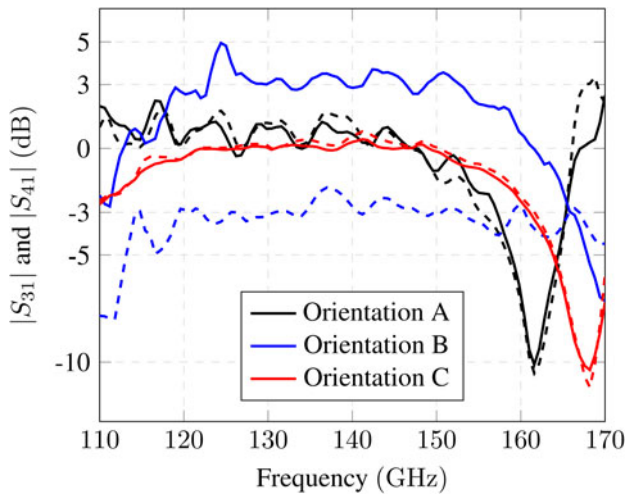


**Fig. 23.** Measured magnitude imbalance between coupling and through paths with source at port 1 and 2 of specimens A, B, and C.

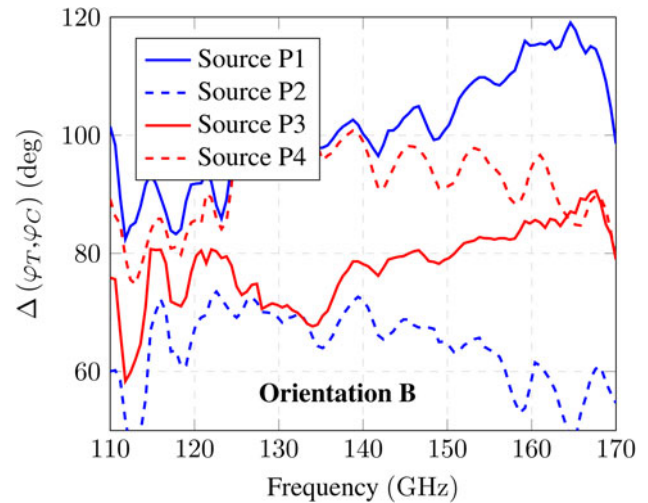


**Fig. 25.** Measured phase difference between through and coupling paths for source at ports 1, 2, 3, and 4 of specimen B.

range of deviations by 0–100 μm at the complex model in Fig. 5 corresponding to a phase variation of  $\Delta\varphi = \beta\Delta l \approx 13^\circ$  at 140 GHz. The solid green line indicates an asymmetry of  $\Delta l = 50 \mu\text{m}$  between the waveguides connecting port 3 and port 4.

**Conclusion**

In this work, the impact of build orientation on additively manufactured hybrid couplers for D-band frequency range has been evaluated and compared to other sources of uncertainties within measurement, instrumentation and additional attached structures for improving measurability. It was found that the impact of geometrical variations as little as 100 μm yield phase errors of about 10°, which is comparable to the variations that are obtained by manual handling of flange interconnects due to varying torque and insufficient planarity. Furthermore, waveguide paths with a length of several millimeters including bends can increase the

attenuation within the measured path by the order of 1 dB already.

Despite this narrow field of tolerances, one specimen could have been realized utilizing the sloped printing-orientation (specimen C), which achieves a measured output magnitude imbalance of as little as 0.7 dB over the frequency range from 120 to 155 GHz and simultaneously, a phase deviation of only < 10° for all combinations of input and output ports. Consequently, the proposed approach is within a suitable range for future applications in the D-band frequency range.

However, next steps should focus on reducing the uncertainties within flange interconnections for 3D-printed components, such as choke flange designs, as well as the elaboration of calibration sets with sufficient quality to remove the impact of measurement extensions to the actual region of interest such as it is the case already with planar PCB and on-chip measurements. Also, an analysis of reproducibility and comparability among different printer systems and resin types will be carried out to improve

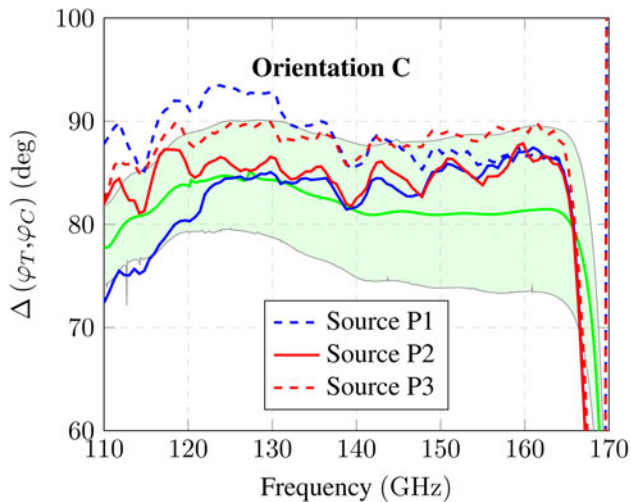


**Fig. 26.** Measured phase difference between through and coupling paths for source at ports 1, 2, 3, and 4 of specimen C as well as simulated range for asymmetry in waveguide feed paths of 0–100  $\mu\text{m}$  with center at 50  $\mu\text{m}$  length difference (green solid).

the applicability of the proposed slotted-waveguide approach. The measurements in this work also show the significance of the specimen orientation within the build volume of DLP-printers for achieving decent performance with the manufactured RF component.

**Acknowledgments.** The authors would like to thank N. Zingraf with the Institute of Microwaves and Photonics for support within manufacturing of the specimens proposed in this work.

## References

1. Bruneau PJ, Janzen HD and Ward JS (2008) Machining of terahertz split-block waveguides with micrometer precision. *2008 33rd International Conference on Infrared, Millimeter and Terahertz Waves*, pp. 1–2. doi: 10.1109/ICIMW.2008.4665435.
2. Lomakin K, Herold S, Simon D, Sippel M, Sion A, Vossiek M, Helmreich K and Gold G (2019) 3D printed slotted rectangular hollow waveguides. *2019 IEEE MTT-S International Microwave Symposium*.
3. Gold G and Helmreich K (2017) A physical surface roughness model and its applications. *IEEE Transactions on Microwave Theory Techniques* PP, 1–13, ISSN: 0018-9480, doi: 10.1109/TMTT.2017.2695192.
4. D'Auria M, Otter WJ, Hazell J, Gillatt BTW, Long-Collins C, Ridler NM and Lucyszyn S (2015) 3-D printed metal-pipe rectangular waveguides. *IEEE Transactions on Components, Packaging and Manufacturing Technology* 5(9), 1339–1349.
5. Shen J, Aiken M, Ladd C, Dickey MD and Ricketts DS (2016) A simple electroless plating solution for 3D printed microwave components. *2016 Asia-Pacific Microwave Conference (APMC)*, pp. 1–4. doi: 10.1109/APMC.2016.7931434.

6. Lomakin K, Herold S, Ringel L, Ringel J, Simon D, Sippel M, Sion A, Vossiek M, Helmreich K and Gold G (2019) SLA printed 3D waveguide paths for E-band using electroless silver plating. *IEEE Transactions on Components Packaging and Manufacturing Technology* 9(12), 2476–2481.
7. Lomakin K, Klein L, Ringel L, Ringel J, Sippel M, Helmreich K and Gold G (2019) 3D printed E-band hybrid coupler. *IEEE Microwave and Wireless Components Letters* 29(9), 580–582.
8. Lomakin K, Sippel M, Ullmann I, Helmreich K and Gold G (2020) 3D printed helix antenna for 77 GHz. *European Conference on Antennas and Propagation*.
9. Lomakin K, Sippel M, Helmreich K and Gold G (2020) Design and analysis of 3D printed slotted waveguides for D-band using stereolithography and electroless silver plating. *2020 IEEE/MTT-S International Microwave Symposium (IMS)*, pp. 177–180. doi: 10.1109/IMS30576.2020.9223819.
10. Lomakin K, Klein L, Sippel M, Helmreich K and Gold G (2021) 3D-printed 3 dB hybrid coupler for D-band applications. *2020 50th European Microwave Conference (EuMC)*, pp. 376–379. doi: 10.23919/EuMC48046.2021.9337997.
11. Cook AM, Joye CD and Calame JP (2019) W-band and D-band traveling-wave tube circuits fabricated by 3D printing. *IEEE Access* 7, 72561–72566. doi: 10.1109/ACCESS.2019.2920291.



and 3D-printed mm-Wave components.

**Konstantin Lomakin** received the B.Sc. degree in electrical engineering from Friedrich-Alexander University Erlangen-Nürnberg (FAU) in 2013, and the M.Sc. degree in information and communication technology from FAU in 2015. He is a member of the Microwave Assembly and Interconnects Group with the Institute of Microwaves and Photonics, FAU. His research interests include signal integrity, EM-modeling,



**Laura Klein** received the B.Sc. degree and the M.Sc. degree in mechatronics from Friedrich-Alexander University Erlangen-Nürnberg (FAU) in 2016 and 2019. Since then she works at the Institute of Microwaves and Photonics of the FAU, doing research on signal integrity, additive manufacturing of RF structures, material characterization, and test.



include 3D-printed microwave components, electromagnetic interaction with non-ideal surfaces, and automation of RF measurements.

**Gerald Gold** received the Diploma degree in mechatronics and the Dr. Eng. degree from Friedrich-Alexander-University Erlangen-Nürnberg (FAU) in 2009 and 2016, respectively. Since 2010, he has been a Research Assistant with the Institute of Microwaves and Photonics, FAU. He became the Group Leader of the Microwave Assembly and Interconnects Group in 2018. His current research interests